Research Square

Preprints are preliminary reports that have not undergone peer review.
They should not be considered conclusive, used to inform clinical practice,
or referenced by the media as validated information.

# MR Imaging and Spectroscopy reveals metabolic changes in glioblastoma driven by treatment with temozolomide and lonidamine

**Tareq Alrashidi**
University of Liverpool
**Sourav Bhaduri**
TCG Crest
**Elisabeth Gash**
University of Liverpool
**Sharifa Alyetama**
University of Liverpool
**Mark Morgan**
University of Liverpool
**Marco Sciacovelli**
University of Liverpool
**Mohesh Moothanchery**
University of Liverpool
**Mahon Maguire**
University of Liverpool
**Lorenzo Ressel**
University of Liverpool
**Harish Poptani**
harish.poptani@liverpool.ac.uk

University of Liverpool

**Article**

**Keywords:** Glioblastoma, Temozolomide, Lonidamine, Magnetic resonance spectroscopy, diffusion weighted imaging, Metabolic reprogramming, Oxidative phosphorylation, Glycolysis, Tumour microenvironment, Seahorse assay, Treatment response, lactate

**Posted Date:** August 7th, 2026

**DOI:** https://doi.org/10.21203/rs.3.rs-10392086/v1

**License:** This work is licensed under a Creative Commons Attribution 4.0 International License.
Read Full License

**Additional Declarations:** No competing interests reported.

# Abstract

Resistance to temozolomide (TMZ) limits the efficacy of treatment in glioblastoma (GBM) and it is fuelled by a metabolic reprogramming of the cancer cells. Lonidamine (LND), a glycolytic and mitochondrial inhibitor, was used in combination with TMZ to evaluate metabolic and microstructural changes in a GBM model. C57BL/6 mice bearing intracranial GL261 tumours were treated with saline, LND, TMZ, or LND + TMZ for five consecutive days. In vivo longitudinal MRI included diffusion weighted imaging (DWI), and lactate-edited $^{1}$H-MRS and the results were confirmed with immunohistochemistry for MCT4 expression. In vitro, acute and chronic bioenergetic reprogramming of GL261 cells was assessed. A significant decrease in lactate was observed in the LND and LND + TMZ groups indicating a change in their glycolytic flux. This metabolic shift was consistent with a marked reduction in MCT4 protein, the lactate transporter. In vitro bioenergetic profiling revealed an acute decrease in mitochondrial respiration, with partial recovery at later time points. Although a limited therapeutic benefit of addition LND to TMZ was observed, its tumour-selective activity and effect on tumour microenvironment seems promising and its long-term effects on tumour development should be investigated as part of an optimized combination strategy for TMZ treatment.


# Introduction

Glioblastoma (GBM) is the most malignant primary brain tumour in adults, characterized by rapid growth, diffuse invasion, and resistance to conventional therapies. Even with advances in resection surgery, radiotherapy, and chemotherapy, the median survival for GBM patients remains around 15 months from the date of initial diagnosis [1]. Temozolomide (TMZ), an oral alkylating agent, is currently the only approved chemotherapeutic agent that is used as an adjuvant to radiotherapy as well as for maintenance therapy. TMZ is cytotoxic, primarily acting through methylation of guanine at the O6 position, resulting in DNA damage and apoptosis [2]. Despite its use in current standard of care for GBM, the clinical utility of TMZ remains constrained by rapid pharmacokinetic clearance, suboptimal intratumoral drug accumulation [3–5], and multifaceted resistance mechanisms rooted in the molecular heterogeneity of GBM [6]. Resistance to TMZ also arises from other mechanisms, including enhanced DNA repair, anti-apoptotic signalling, and metabolic reprogramming. For instance, TMZ-resistant cells demonstrate a heightened reliance on glycolytic flux, supported by GLUT3 overexpression, to fuel antioxidant defences and drug efflux compared to sensitive counterparts, which allow tumour cells to tolerate cytotoxic stress. Even in tumours that initially respond, resistance invariably develops during treatment, leading to recurrence and poor prognosis [7, 8].

Bevacizumab is the only other FDA-approved systemic therapy for recurrent GBM besides TMZ, but recent data showed that it does not improve overall survival [9]. Hence, there is a desperate need for a new therapeutic approach to overcome TMZ associated resistance.

The tumour microenvironment (TME) is a complex ecosystem where interactions between the tumour, stromal and immune cell populations promote adaptive responses including metabolic reprogramming,

immune evasion, and enhanced DNA repair capacity [6, 11, 12]. Altered energy metabolism in the tumour, specifically the Warburg effect, generates lactate, leading to extracellular acidification. This promotes angiogenesis, immune evasion, and invasion, aiding further proliferation and reduced host survival [13]. Furthermore, the TME has additional distinctive microenvironmental cues that vary based on tumour type, tissue, and stage such as oxygen levels and pH. Therefore, altering energy metabolism and tissue pH could represent a strategy to increase the effectiveness of drugs such as TMZ, which is also pH-sensitive and activated at physiological pH [14, 15]. In this context, the identification of metabolic vulnerabilities linked to TMZ resistance represents a viable therapeutic avenue.

We have previously demonstrated that targeting the choline metabolism in GBM using MN58b in combination with TMZ, is cytostatic with reduced tumour cell proliferation [10]. We therefore aimed to explore modulation of other metabolic processes as potential therapeutic targets for treatment of resistant and recurrent GBM. Lonidamine (LND) is a metabolic inhibitor that disrupts mitochondrial respiration and lactate efflux through inhibition of hexokinase II, the mitochondrial pyruvate carrier (MPC), and monocarboxylate transporters (MCT1/4), potentially in a dose-dependent manner (notably, the $IC_{50}$ for MPC inhibition is approximately one order of magnitude lower than that required for the inhibition of the MCTs) [16, 17]. LND possesses the capability to sensitize chemotherapy and radiotherapy by depleting cellular ATP and inducing intracellular acidification, thereby hindering processes essential to DNA synthesis, repair together with cell proliferation and survival [15, 16]. While LND alone has been shown to have modest antitumour activity in GBM [18], we hypothesised that its metabolic and pH-altering actions can modulate TMZ activation, uptake, and potency within cancer cells and affect also the TME. LND also displays favourable pharmacological characteristics for cancer treatment compared to other conventional anticancer agents; it does not cause bone marrow suppression, alopecia, or mucosal necrosis, and lacks mutagenic effects on somatic and germline cells [19]. Furthermore, LND demonstrates tumour selectivity at doses below 400 mg/m² with minimal toxicity in normal tissues [18], making it an attractive adjuvant for multimodal therapy. Since LND induces tumour de-energisation by depleting intracellular ATP, it may suppress energy-dependent efflux mechanisms, thereby enhancing TMZ retention and activity [19, 20].

Glycolysis is a key metabolic process for cancer cells. Indeed, through increased glycolytic flux, cancer cells generate building blocks for cell replication, de novo amino acids, lipids and NADPH to maintain the redox balance (21). More recently, it has been proposed that the enhanced glycolysis observed in cancer cells is also key for $NAD^+$ regeneration with hexokinase localisation being an important regulator of the glycolytic switch observed in cancer (22, 23). Changes in intracellular and extracellular acidification, bioenergetic and anabolic alterations together with redox imbalance derived from disruption of glycolysis by LND could inhibit DNA repair and drug resistance pathways, whereas TMZ induces cytotoxicity through DNA alkylation. A combination of treatment with LND and TMZ could therefore provide a synergistic treatment efficacy, addressing both genomic and metabolic vulnerabilities and delaying the onset of treatment resistance [24, 25].

This study aims to evaluate the therapeutic efficacy of combining LND and TMZ in vivo using a GL261 GBM syngeneic mouse model and in vitro using GBM cell lines. We utilised multiparametric MRI, including $T_2$-weighted imaging, intra voxel incoherent motion (IVIM)-DWI, conventional $^1$H-MRS, and lactate-edited MRS, to examine microstructural and metabolic alterations throughout treatment. We hypothesized that metabolic modulation by LND alters cancer cell's metabolic features, thereby influencing TMZ activation and its therapeutic efficacy. A better understanding of this interaction may inform the development of combination strategies to improve GBM treatment.

## Materials and Methods

All animal experiments were carried out in compliance with the UK Animals (Scientific Procedures) Act 1986 as amended in 2012 and were approved by the University of Liverpool Animal Welfare and Ethical Review Board. All experiments are reported following ARRIVE principles. A total of 84 male C57BL/6 mice (Charles River, UK; age:8–12 weeks, weight:18–22g) were used in the study; tumours were successfully established in 64 animals, while 20 animals either failed to develop tumours or were euthanized prior to imaging. Male mice were used to enable comparison with prior GL261/TMZ and TMZ combination therapy studies [10, 26, 27], and to reflect the 1.6-fold higher incidence of GBM in male patients [28]. The animal was anaesthetized using 2% isoflurane in $O_2$, and a rectal probe and respiratory pillow were used to monitor body temperature and breathing rate. The animal was secured using a stereotaxic frame, and a burr hole drilled 2.0 mm posterior to the bregma and 1.5 mm to the right. GL261 GBM cells ($2.5\times10^5$; ATCC, USA) suspended in 5μL of serum-free media were injected into the right brain cortex at a depth of 2.0 mm from the surface.

# Drug treatment of mice bearing GL261 GBM

Animals that successfully developed tumours (n = 64) were randomly divided into four groups: saline control (n = 20), LND (n = 15), TMZ (n = 15), and a combination therapy group (LND + TMZ, n = 14). The sample size was determined based on group sizes used previously [10, 29]. All animals received their treatment regimen every day for five consecutive days. Treatment commenced when tumours exceeded 2.0 mm in diameter, typically 10 days post-implantation, with tumour diameter assessed using MRI. The control group received intraperitoneal injections of saline, the LND group received 100 mg/kg of LND intraperitoneally [30], the TMZ group received 50 mg/kg TMZ orally via gavage [28], and the combination (LND + TMZ) therapy group received both LND and TMZ treatments as above. The dosing schedule and treatment duration were selected based on previously established preclinical GBM studies that demonstrated metabolic and therapeutic responses to LND and TMZ in mice [30–36].

## MR Scanning

A 9.4 T Bruker 94/20USR scanner equipped with 440 mT/m imaging gradients was used for all imaging studies (Bruker BioSpin, Germany). An 86 mm quadrature birdcage coil was used for transmission, and a

4-channel phased array surface coil for signal reception (Bruker BioSpin, Germany). Animals were anaesthetized and monitored as described above, with body temperature maintained using a heated water blanket; respiration rate and body temperature was monitored throughout the scanning process using an SA Instruments monitoring unit (SA Instruments, NY, USA). Animals were scanned at baseline (day 0), during therapy (day 3), and at the end of treatment (day 6). $T_2$-weighted images, single voxel PRESS spectra (with/without water suppression), single voxel ISIS-SelMQC spectra (single, and zero+double quantum) and IVIM-DWI images were acquired at each time point. To monitor tumour volume and for spectroscopic voxel placement, $T_2$-weighted (RARE) images were acquired (TR/TE/echo spacing = 3497/33/11 ms, 2 averages, 33 slices, 0.3 mm slice thickness, FOV=25x25mm$^2$, 256×256 matrix, RARE factor = 8, BW = 42 kHz, acquisition time = 3 minutes 50 seconds per scan). A 2x2x2 mm³ PRESS voxel was placed within the tumour, field map-based shimming was performed to ensure FWHM < 20 Hz (Mapshim, Bruker), and a $^1$H spectrum acquired (TR/TE = 2000/16.5 ms, 200 averages, 2048 points, spectral width = 4401 Hz, VAPOR water suppression, acquisition time = 6 minutes 40). Using the same voxel location and dimensions, an ISIS-SelMQC sequence was used to detect the lactate signal [34, 35]. Sequence parameters were TR = 2000 ms, 32 averages, 2048 points, 8012 Hz spectral width, acquisition time = 8 minutes 32 seconds per scan. IVIM DW-MRI was acquired employing a spin echo sequence with segmented echo planar imaging readout (TR/TE = 1800/24.67 ms, no. of segments = 6, FOV = 20×20 mm$^2$, 96x96 matrix, 1.0mm slice thickness, 1 mm slice gap, 8 slices, no. of averages = 2, diffusion gradient duration/separation = 4.5/10.6 ms, acquisition time = 15 minutes 50 seconds per scan). Axial images were acquired with 5 $A_0$ images and 13 b-values (20, 30, 40, 50, 60, 80, 140, 230, 350, 570, 840, 1120, 1460 s/mm$^2$) in 3 orthogonal directions. The total imaging time per animal at each time point was approximately 40 minutes including setup and shimming.

# Data Analysis

Tumour volumes were measured from the $T_2$-weighted images by manually contouring the tumour boundaries on each slice utilizing ITK-Snap (version 4.2.0; www.itksnap.org) The areas of the contoured region were multiplied by the slice thickness to calculate tumour volume.

PRESS data were preprocessed using jMRUI 5.2 (www.jmrui.eu), including residual water removal (HLSVD) and apodization [39–41]. A metabolite basis set (including tCho, NAA, Glx, Lip + Lac, tCr, mI + Gly, and additional metabolites) was simulated using the NMRScope tool within jMRUI [42], and metabolite resonances were fitted using the QUEST algorithm [43, 44]. Further details of the PRESS-MRS spectral processing, fitting procedures, and basis-set simulation have been described previously [45]. Cramér–Rao lower bound (CRLB) criteria were employed to evaluate the quality of the fitting. A threshold of 20% was employed for CRLB; fitted metabolite resonances that had a CRLB above this value were deemed poorly fitted and excluded from further analysis. The integrals of the water and lactate signals wee integrated from the single quantum, and zero + double quantum, SelMQC spectra using Topspin v.3.1 (Bruker). The ratio of the lactate/water integrals was used as a relative measure of lactate concentration.

## Parameter Calculation

IVIM-DWI data were processed using an in-house pipeline developed in MATLAB 2021a (MathWorks, USA). The data were fitted on a pixel-by-pixel basis using the Levenberg-Marquardt algorithm [46]. Voxel-wise values of IVIM-DWI parameters *D*, *D**, and *f* were calculated. The IVIM-DWI and $T_2$-weighted images were used to identify imaging slices containing the tumour, and a region of interest (ROI) was manually contoured to cover the entire tumour; ROIs used for IVIM parameter estimation were manually delineated on the b = 0 image from the EPI sequence.

## Seahorse Mito Stress Test Assays

The Seahorse assay enables real-time measurement of cellular bioenergetics by simultaneously quantifying mitochondrial respiration and glycolytic rate [47]. An XFe96 Seahorse Extracellular Flux Analyzer (Agilent Technologies; Santa Clara, CA, USA) was used to assess mitochondrial respiration and glycolytic rate by measuring oxygen consumption rate (OCR) and extracellular acidification rate (ECAR) of GL261 GBM cells via the Mito Stress Test Assay. Seahorse XF Base Medium was supplemented with 4.5g/L glucose, 2mM glutamine and 1mM sodium pyruvate to match the cell culture media. The Seahorse assay media was prepared at pH 7.4 following the manufacturer's instructions. Cells were seeded in XF96 microplates at a density of 26,000 cells per well (12 replicate wells per treated group) and allowed to adhere overnight. To assess acute changes in respiration due to treatment (~ 30 mins), three basal OCR and ECAR measurements were taken in a repeating 3-0-3 mix-wait-measure cycle, with each cycle consisting of 3 minutes of mixing to equilibrate the assay medium, 0 minutes of waiting, and 3 minutes of active data measurement. After basal measurements, LND, TMZ and LND + TMZ (350 μM, 150 μM, and 350 + 150 μM, respectively) were injected into the wells, and measurements taken for 20 minutes. Then, 1 μM oligomycin (inhibitor of mitochondrial ATP synthase) was injected into the wells, and three measurements were taken. Next, 0.5 μM FCCP (uncoupler of the proton gradient across the inner mitochondrial membrane to drive oxygen consumption to its maximum capacity) was injected and three measurements were taken. Lastly, a combined rotenone/antimycin A solution (1 μM each) was added to inhibit Complexes I and III, thereby allowing for the quantification of non-mitochondrial oxygen consumption over three measurements. For chronic treatment conditions, cells were pre-treated with LND and/or TMZ, either as single agents or in combination, for 24 h or 72 h prior to Seahorse analysis, for low (LND: 175 μM, TMZ: 75 μM and LND + TMZ: 175 μM + 75 μM) and high dose regimens (LND: 350 μM, TMZ: 150 μM and LND + TMZ: 350 μM + 150 μM). These drug concentrations were based on similar experiments reported earlier using LND and TMZ [17, 48]. Metabolic rates (OCR and ECAR) were recorded throughout the assay and then normalised to total protein content determined by a BCA assay. This normalisation expresses metabolic activity per unit biomass, ensuring that these metabolic readouts are biologically meaningful rather than just technical outputs. $J_{ATPglyc}$ (the glycolytic ATP production rate derived from ECAR) and $J_{ATPox}$ (the mitochondrial ATP production rate derived from OCR) production rates were calculated (in units of pmol ATP/min/μg protein) using the method

described by Mookerjee et al., [49] which converts extracellular flux measurements into ATP production rates by accounting for proton production and buffering capacity.

# Histology and Immunohistochemistry

Following completion of treatment and imaging on day 6, three animals from each group were sacrificed via an intraperitoneal injection of 3 mL/kg pentobarbital sodium (Euthatal, Merial Animal Health Ltd, Harlow, UK). The aorta beneath the diaphragm was severed by making an incision into the abdomen along the mid-ventral line. A 25-gauge needle attached to an extension tube was inserted into the heart's left ventricle and secured with a clamp. The heart was initially perfused with 30 mL of PBS, followed by 30 mL of 4% Formalin (Sigma-Aldrich, St. Louis, MO). Brains were then extracted and immersed in 4% formalin for fixation. Fixed brains were embedded in paraffin and sliced in approximately 2 mm-thick transverse sections at the tumour site. Hematoxylin and eosin staining was performed on 4 µm thick slices containing tumours and adjacent brain tissue. An average number of mitotic figures was computed per high power field (HPF: 400x magnification; ocular FN: 22; objective 40×/0.65HPF). The mitotic index was evaluated as the number of mitotic figures in five randomly selected HPFs at the interface of the tumour and the surrounding brain (infiltrating margin).

For immunohistochemistry (IHC), formalin-fixed paraffin-embedded sections were placed in a BOND-MAX Automated Immunohistochemistry Vision Biosystem (Leica Microsystems GmbH, Wetzlar, Germany) for standardized staining. First, tissues were deparaffinized and subjected to heat-induced antigen retrieval using Epitope Retrieval Solution 2 (EDTA-buffer pH 8.8) at 98°C for 20 min. Following washing, peroxidase blocking was carried out for 10 min using the Bond Polymer Refine Detection Kit DC9800 (Leica Microsystems GmbH).

Following a second wash, tissue sections were incubated with the primary antibody against MCT4 (recombinant rabbit monoclonal [EPR28177-30], 1:200) for 30 min. This was followed by incubation with a polymer for 10 min. The reaction was visualized with 3,3'-diaminobenzidine (DAB-Chromogen) for 10 min to produce a brown chromogenic precipitate. Sections were then counterstained with Haematoxylin for 5 min, rinsed in deionized water for 5 min, dehydrated and coverslipped. For IHC quantification, MCT4-stained slides were digitized using an automated high-resolution digital slide scanner at 20× magnification. The resulting whole-slide image analysis was undertaken using QuPath software (v.0.5.1). Briefly, the tumour area was manually annotated as the region of interest (ROI), ensuring inclusion of the tumour area while excluding healthy brain parenchyma. Cells within the ROI were identified and categorized based on the intensity of the 3,3'-diaminobenzidine (DAB) reaction product, which marks the site of MCT4 protein expression. Positive cell detection parameters were applied uniformly across all experimental groups to ensure consistency. To provide a granular assessment of protein expression, cells were classified into four intensity categories based on their DAB signal: negative (blue), weak (yellow), moderate (orange), and strong (red) staining. The QuPath software automatically calculated the total cell count and the percentage of cells within each intensity category for the entire ROI. These classifications were then utilized to calculate a quantitative H-score for each sample.

# Statistical analysis

Analysis of Variance (ANOVA) was performed to evaluate differences among treatment and control groups (% change in tumour volume, IVIM parameters, and metabolite ratios on day 3 and day 6 with respect to baseline values). Bonferroni's post hoc test was used to adjust the p-value, accounting for the total number of comparisons made. The overall percentage survival was estimated using Kaplan-Meier curves. MATLAB and Prism version 10.2.0 (GraphPad, USA) were employed for all analyses. Data are presented as mean and ± standard deviation (SD), and differences in groups were considered statistically significant if $p < 0.05$.

## Results

# Tumour Volume Assessment

Tumour volume was monitored by $T_2$-weighted MRI (Fig. 1A), normalized to baseline volumes for group comparisons and reported as a percentage change on days 3 and 6 (Fig. 1B). At baseline, the tumour volumes for the saline control (3.3 ± 3.1 $mm^3$), LND (3.1 ± 2.6 $mm^3$), TMZ (2.6 ± 2.3 $mm^3$), and LND + TMZ (3.2 ± 1.9 $mm^3$, Table 1) were not significantly different ($p > 0.05$). On day 3, all groups exhibited moderate tumour growth, with no significant differences between groups (Table 1). After 6 days of treatment, tumour volume had increased in all groups: Saline (21.1 ± 17.1 $mm^3$), LND (21.9 ± 9.97 $mm^3$), TMZ (20.5 ± 16.7 $mm^3$), and LND + TMZ (18.5 ± 9.72$mm^3$), Table 1. Taken together, the acute effect of the combined treatment does not alter the tumour volume of GBM in vivo.

# Survival

Survival was assessed via Kaplan–Meier analysis (Fig. 1C). The control (grey) and LND monotherapy (red) groups had the lowest survival rate, reaching nearly 60% mortality by day 6 in both groups The TMZ group (blue) showed improved survival compared to the control and LND groups (80%), the LND + TMZ combination group (green) exhibited a promising trend of improved survival, even though this was not statistically significant, showing a delayed onset of mortality relative to the other groups with 100% animals surviving up to day 4 (Fig. 1C).

# Metabolic Alterations Assessed by $^1$H-MRS and Lactate-Edited MRS

$^1$H-MRS demonstrated notable changes in tumour metabolism with treatment. While lactate signals assessed using ISIS-SelMQC edited MRS were comparable in all cohorts (saline control, LND, TMZ and LND + TMZ) at day 0 (Fig. 2.B-E), the lactate/water ratio was significantly lower in LND and LND + TMZ treated groups than saline control and the TMZ treated group at days 3 and 6 ($p < 0.05$ in all cases, Fig. 2.B-F, Table 1). Following treatment with LND or LND + TMZ, the lactate resonance was undetectable at days 3 and 6. TMZ only treatment group had no significant change in lactate/water ratio compared to the control group across all timepoints ($p > 0.05$, Fig. 2F). tCho/NAA ratio was significantly lower in both the

TMZ only and LND + TMZ treatment groups relative to the saline control group on day 6, with the largest difference observed in the LND + TMZ treatment group (1.46 ± 0.15 and 1.41 ± 0.34 vs. 1.92 ± 0.44; $p < 0.05$; Table 1, Fig. 3A).

# Diffusion and Perfusion Imaging with IVIM-DWI

IVIM-DWI-based parameters were normalized to baseline values for comparison between treatment groups. *D*, *D**, and *f* were not significantly different between treatment groups either at day 3 or at day 6 ($p > 0.05$, Fig. 4C, Table 1). In the presence of metabolic differences resulting from differing treatment strategy evidenced by MRS, the lack of significant variation in *D*, *D**, and *f* values with treatment indicates IVIM parameters are less responsive to early therapeutic changes under the treatment regimen used in this study.

# Seahorse Mitochondrial Stress Test Assay

Since the in vivo results showed a significant reduction in lactate (Fig. 2) at early time points (3–6 days), we measured the effect of the combination of LND and TMZ in vitro using GL261 cells to understand if this effect is caused by bioenergetic changes specifically in the tumour cells. Figure 5 shows representative OCR and ECAR profiles of GL261 cells with LND alone or in combination with TMZ after acute (~ 30 min) to capture immediate drug responses, and chronic treatment (72 hrs) that mimics the timeline of the changes observed in vivo.

This assay enables estimation of the balance between glycolytic flux, mitochondrial oxidative metabolism for ATP generation together with measurement of cellular respiration (oxygen consumption rate OCR) as a readout of the mitochondrial functioning and extracellular acidification rate (ECAR) mainly linked to lactate production. In the acute phase of treatment (Fig. 5A), all treatment groups exhibited a similar basal respiration rate (values expressed in pmol $O_2$ / min / µg protein), and therefore mitochondrial activity, prior to drug administration (control: 9.13 ± 2.53; LND: 8.20 ± 3.33, $p > 0.05$; TMZ: 9.38 ± 2.33, $p > 0.05$; LND + TMZ: 7.28 ± 2.35, $p > 0.05$, Table 2). Following acute treatment (~ 30 min), cells exposed to high concentrations of LND either alone, or in combination with TMZ, demonstrated a significant reduction in $J_{ATPox}$ values (expressed in pmol ATP / min / µg protein) calculated from oxygen consumption rate (OCR) relative to control and TMZ alone treated GL261 cells (LND: 12.75 ± 14.73; LND + TMZ: 10.48 ± 7.78 vs. Control: 43.78 ± 12.51 and TMZ: 44.78 ± 11.60; $p < 0.0001$; Table 2, Fig. 6A). TMZ treatment alone did not significantly alter $J_{ATPox}$ relative to control. Even though not significant, $J_{ATPglyc}$ values from glycolysis, calculated using the extracellular acidification rate (ECAR), showed a marginal increase in $J_{ATPglyc}$ values (expressed in pmol ATP / min / µg protein) following LND treatment that was absent in control or TMZ-only treated cells (LND: 6.75 ± 2.80; LND + TMZ: 6.33 ± 2.73 vs. Control: 2.85 ± 3.60 and TMZ: 1.15 ± 1.00 ; $p > 0.05$), suggesting a potential temporary compensation by glycolysis (Table 2) consistent with higher ECAR value observed in Fig. 5A. In the chronic treatment experiments (24 h and 72 h treatment), $J_{ATPox}$ values in LND- and LND + TMZ-treated cells increased relative to their respective acute time points at high drug concentrations by approximately 182% at 24 h (36.1 ± 19.8) and 194% at 72 h (37.5 ± 17.8) in the LND group, and 198% at 24 h (31.2 ± 20.6) and 196% at 72 h (31.1 ±

8.68) in the LND + TMZ group, suggesting a partial recovery in mitochondrial oxidative metabolism following inhibition with LND, although these increases did not reach statistical significance ($p > 0.05$) (Fig. 6B, Table 2). For cells treated with the lower concentration of LND at both 24 and 72 h time points, $J_{ATPox}$ values approximately doubled in the LND and LND + TMZ groups compared to the high concentration treatment groups (Fig. 6C, Table 2) suggesting a concentration dependence for the treatment effect. $J_{ATPox}$ in both the LND and LND + TMZ groups values under chronic treatment conditions were not significantly different from control or TMZ treated cells, indicating metabolic recovery over time. No significant differences in glycolytic ATP production ($J_{ATPglyc}$) were observed in the LND or LND + TMZ groups compared to control or TMZ treated cells under chronic conditions.

# Histopathological analysis

Histological analysis for cell proliferation (mitotic index) and protein expression (MCT4 H-score) was performed after the final imaging time point (day 6) on three animals from each group. Representative stains and corresponding digital intensity heatmaps are shown in (Fig. 7A).

While not statistically significant, a lower mitotic index was observed for TMZ and LND + TMZ-treated animals relative to both control and LND-treated animals. (Table 2, Fig. 7B, left). However, a marked lower level of MCT4 protein expression was observed in groups receiving LND. Specifically, the MCT4 H-score was significantly lower in the combination (LND + TMZ) therapy group compared to the saline control ($7.33 \pm 1.24$ vs. $67.2 \pm 15.7$; $p < 0.05$, Table 2, Fig. 7B, right), representing suppression of MCT4 expression in response to LND treatment.

Notably, LND monotherapy also demonstrated a substantially lower level of MCT4 expression ($25.1 \pm 19.1$) compared to both saline and TMZ monotherapy, albeit not statistically significant (Table 2, Fig. 7B, right). These results indicate that treatment with LND and reduce lactate levels in the TME might be linked to reduced MCT4 expression and subsequent reduced release of lactate in the TME by cancer cells.

# Discussion

In this study, we explored the use of inhibitors targeting cancer cell metabolism as part of an adjuvant strategy to maximise the effect of TMZ in GBM and mitigate the risk of chemoresistance. Specifically, we investigated the effect of LND as an adjuvant to TMZ in the treatment of GL261 GBM. We observed that treatment with LND, either in isolation or in combination with TMZ, resulted in a significant reduction in tumour lactate levels to below detection limits in vivo within a short timeline (3–6 days). Such an effect starts to be become apparent after three days of treatment, while no significant change in other measured metabolites or MRI parameters was observed. As we only used a specified dose regimen, we cannot fully describe the underlying mechanism or assess all the consequences of this lactate reduction. However, we postulate that the decrease in lactate could be driven by a direct effect of LND on cancer cells or be due to the result of broader reprogramming of the tumour microenvironment. However, within this short time period, the treatment does not reduce tumour growth or improve animal

survival. These results suggest that changes in lactate levels arise earlier but assessing their full impact on the tumour development might require a longer timeline and could involve other cells present in the TME such as glioma stem cells (GSCs) and immune cells.

Intriguingly, on day 6 post-treatment, we also observed significantly lower tCho/NAA ratios in both the TMZ and combination therapy groups relative to control tumours, with the combination therapy group exhibiting the larger effect. The LND-only group revealed a modest change in tCho/NAA. The markedly lower tCho/NAA ratio in only the TMZ-treated cohorts suggests that the decline in tCho/NAA is primarily due to TMZ, and it is consistent with our previous study [10].

To assess if the effect of the LND on lactate is driven primarily by cancer cells, we studied the bioenergetics of the GBM cells in vitro in the presence of LND and TMZ. A critical challenge for the interpretation of these results is the inherent metabolic plasticity of cancer cell, and particularly GBM cells. Tumours can readily shift between glycolysis and oxidative phosphorylation (OXPHOS) based on microenvironmental conditions, or maintain a hybrid metabolic state [12, 50, 51]. This adaptability enables drug resistance to both glycolytic inhibitors and DNA-damaging agents [8]. LND has been shown to exert cell-line–dependent metabolic effects as reported in melanoma (DB-1 > WM983B) and prostate cancer (PC3 > CWR22Rv1) models, with more “energetic” tumour phenotypes exhibiting greater ATP depletion and chemo-sensitisation than less energetic lines following LND treatment [33, 34]. These studies demonstrated LND to consistently precipitate an acute mitochondrial crisis marked by a lower β-NTP/$P_i$ ratio observable with $^{31}$P-MRS, and suppressed $J_{ATPox}$ in Seahorse assays. This was accompanied by a transient compensatory increase in $J_{ATPglyc}$ and consequent intracellular lactate/$H^+$ accumulation due to impaired MCT1/4-mediated export [33, 34]. Such observations are in agreement with our findings of impaired mitochondrial ATP production in the acute phase of treatment in vitro where we observed a transient increase in glycolytic activity, consistent with disrupted ATP homeostasis, and metabolic stress. This is likely due to the dose-dependent effect of LND on the pyruvate transporter. Importantly, as in the work by Orlovskiy et al., our in vitro data show that tumour cells that survive the initial treatment with LND reprogramme their bioenergetics to a more OXPHOS-dependent state with reduced glycolytic contribution, often replaced by alternative substrates, such as glutamine or fatty acids, and associated metabolic plasticity [34, 52–54]. This could also represent another therapeutic dependency worth exploring.

The reduction in lactate that we observed in vivo is also compatible with a decrease in expression of lactate transporter MCT4. MCT4 overexpression is a recognized hallmark of a glycolytic cancer phenotype and LND treatment induced a marked inhibition of MCT4 transporter expression within the tumour tissue, particularly in the combination therapy group. It should be noted, however, that while MCT4 is a primary exporter of lactate from glycolytic cells, lactate export is a process that can also be mediated by other MCT isoforms, such as MCT1, which might be highly plastic and dependent on the metabolic state and pH gradient of the tumour microenvironment. These findings also propose LND’s specificity for MCT4 (within the range of the concentrations used in the study), confirming that its metabolic impact might be directly mediated from the targeted disruption of this lactate exporter. Our in

vitro and in vivo data support the idea that LND primarily induces metabolic reprogramming rather than sustained energetic collapse, or inhibition of DNA repair. The resulting low-proliferation, OXPHOS-dominant, state is likely to be less susceptible to TMZ-induced replication-dependent cytotoxicity [55, 56], which may explain why LND failed to enhance TMZ efficacy despite significant metabolic modulation, specifically in glycolysis. This interpretation is consistent with reports in prostate cancer, where LND induced remarkable metabolic changes yet did not confer additional therapeutic benefit when combined with radiotherapy [31]. Taken together, our data suggest that LND decreases mitochondrial respiration followed by a transient increase in extracellular acidification while chronic LND showed a mitochondrial recovery increase of respiration after 3 days, compatible with a LND's biphasic effects in GBM. In vivo, the main biochemical highlight of LND after 6 days post-treatment is the decrease of lactate in the tumour and TME. While an acute MPC blockade could impair pyruvate oxidation and affect the cellular oxidative metabolism, the suppression of MCT4 impairs lactate release as part of a more complex metabolic adaptation. As shown by the dramatic downregulation of MCT4 export machinery, surviving GBM cells may downregulate glycolysis, and consequently pyruvate generation, to limit intracellular lactate accumulation and finally avoid aberrant intracellular acidosis. Glucose re-routing into upstream pathways such as the Pentose Phosphate Pathway (PPP), and serine/glycine synthesis, and other anabolic processes is key for cancer cells, shifting mitochondrial ATP production to other substrates such as glutamine or fatty acids. This rewiring sustains proliferation, and it is possible that the consequences of these alterations require more time to impact tumour growth in vivo, explaining LND's lack of antitumor efficacy despite significant metabolic perturbation. The Seahorse Extracellular Flux analysis enables real-time, non-invasive measurements of OCR ($J_{ATPox}$) and ECAR ($J_{ATPglyco}$), allowing comprehensive metabolic profiling of drug responses in cells [47, 57]. Future studies should employ Seahorse Fuel Flex assays to determine compensatory substrate utilization (e.g., glucose, glutamine, fatty acids), as well as use $^{13}C$ MRS for an assessment of pyruvate to lactate conversion, both of which may help guide rational co-targeting strategies. In this context, it would be critical to test the effect of LND in vitro at 6 days to compare those results with those obtained in vivo and also measure the lactate levels and LND impact on the tumour growth in vivo at longer end-points to have a complete evaluation of the LND efficacy.

Our findings also underscore the importance of tumour metabolic plasticity and suggest that LND treatment may also require optimized regimens or co-targeting of the processes that use other substrates (glutamine or fatty acid oxidation metabolism) to fuel GBM growth [58].

Previous studies have reported that IVIM-derived parameters can serve as early biomarkers of response to treatment in IDH-wildtype GBM treated with chemoradiation, even when conventional diffusion or perfusion measurements did not evidence treatment response [59]. This suggests that IVIM-DWI has the potential to detect subtle microstructural or physiological changes before anatomical or volumetric changes become apparent. However, despite considerable metabolic changes, no significant differences were observed in tumour volume, survival or IVIM-derived parameters (D, D*, f) between treatment groups in the present study. These results likely indicate a state of metabolic stress or early adaptive

cellular reprogramming in response to therapy, rather than cytotoxicity. LND treatment did not significantly alter perfusion-related IVIM metrics (D*, f), consistent with previous studies using laser Doppler imaging that detected no significant changes in systemic blood flow after LND administration [60]. This implies that, LND treatment with the dose regimen used in our study does not exert significant effect on tumour vasculature, and that its metabolic inhibitory effect is independent of changes in tumour perfusion. Treatment with TMZ did not demonstrate significant changes in IVIM-perfusion-related parameters compared with other cohorts, consistent with previous in vivo and in vitro studies [10, 61].

An interesting observation of our study is the absence of an additive effect in the combination group, which may be explained by the known relationship between intracellular pH and the activation of TMZ. Although TMZ is chemically stable under acidic conditions, conversion to MTIC, its active form, is achieved through base-catalysed hydrolysis, which is optimal at physiological pH (~ 7.4) [62]. To elucidate the role of pH on the antitumor effect of TMZ, Stéphanou and Ballesta developed a mathematical model using U-87 MG cells. In this model, the cellular, spatial and pH heterogeneity of the tumour microenvironment were examined. The authors found that, in all scenarios, optimal TMZ efficacy was obtained when the pH of tumour cells was close to physiological pH values [62]. Even though we did not directly measure intracellular pH (pHi) in our study, previous literature utilising $^{31}$P-MRS has firmly established that LND induces acute significant intracellular acidification in tumour cells [20, 30, 33, 34, 60]. While this initial intracellular acidification is effective in disrupting tumour metabolism, it could paradoxically inhibit TMZ activation during this early phase. This may account for the absence of additive treatment efficacy in the combination treatment group. These observations point to the need for $^{31}$P-MRS as an additional readout since it can aid in quantifying ATP, phosphocreatine and intracellular pH (pHi), which may enable the optimal timing and sequencing of combination therapies [60; 63].

In GBM, MGMT promoter methylation status and mismatch repair (MMR) integrity are key determinants of TMZ sensitivity [64–67]. These molecular characteristics were not assessed in the GL261 model used in this study. Given the suboptimal response to TMZ observed here, future studies should incorporate MGMT and MMR profiling to better interpret TMZ sensitivity and evaluate potential combination effects with LND. Lactate is a reactive molecule capable of a novel protein post-translational modification called lactylation [68]. The impact of this on the broad epigenetic status of the cancer cells including indirect effects on DNA methylation is still unexplored.

Collectively, our results highlight the sensitivity of non-invasive metabolic imaging in identifying post treatment changes, even in the absence of volumetric changes. The rapid suppression of lactate and decrease in choline metabolism indicate that LND and TMZ are capable of inducing early metabolic stress in GBM, even though they may not have the desired therapeutic effect with the present treatment protocol. These results validate the practicability of incorporating MRS and IVIM-DWI into standard preclinical workflows. The results suggest longer treatment regimens or adjusted dosing schedules may be needed. Alternatively, rational combination strategies simultaneously targeting multiple metabolic pathways in GBM could help to overcome metabolic plasticity, increase tumour vulnerability, and

ultimately enhance overall therapeutic efficacy. The observed metabolic adaptations in GL261 tumours suggest that this model recapitulates key features of the metabolic plasticity and therapy resistance characteristic of clinical GBM, highlighting its value as an appropriate preclinical tool for investigating mechanisms of treatment resistance.

The dose regimen used for LND in this study was based on previous work on subcutaneous tumour models [30], which may not fully capture the complexity of orthotopically implanted intracranial GBM. The blood-brain barrier likely limits drug penetration and lowers effective concentrations in the tumour, potentially explaining the limited treatment success observed in our study. Additionally, the aggressive nature of the GL261 model necessitated a short imaging window, restricting evaluation of long-term treatment effects. Future work could investigate using lower tumour implantation loads allowing a longer study period to better observe survival, and lasting metabolic changes with LND + TMZ treatment.

These data were obtained from an established rodent GBM cell line, which develops large tumours within a short period. While such models are useful for rapid experimental evaluation, their accelerated growth rate limits how well they represent the human GBM. Therefore, extrapolating these findings to the clinical setting should be performed with caution. Future studies could consider using human-derived xenograft models, such as U251, which may more closely mimic the time course of tumour growth and therapy resistance characteristic of human GBM. PDX models also present substantial challenges, as they rely on immune-deficient rodents and therefore fail to fully recapitulate the tumour–immune interactions and microenvironmental complexity of human tumours.

## Conclusion

Our findings indicate that magnetic resonance spectroscopy (MRS) can detect early metabolic alterations induced by LND + TMZ treatment. Our data suggest that more time is required to evaluate the long-term consequences of the lactate decrease observed in the tumour microenvironment in vivo which was detected as early as day 3 and remains sustained through the last imaging time point at day 6 (end of treatment). LND tumour-selective activity and low toxicity toward normal tissues highlight its potential as a valuable adjunct to TMZ therapy which should be further characterised. By preferentially targeting tumour metabolism, LND may enhance treatment efficacy while reducing the risk of off-target toxicity, supporting its continued evaluation in combination therapeutic strategies.

## Declarations

# Funding:

Tareq Alrashidi was funded by a PhD studentship grant from the Ministry of Education, Saudi Arabia. Sharifa Alyetama has been funded by a PhD studentship grant from the Ministry of Health, The State of Kuwait. Elisabeth Non Gash was funded by a PhD studentship grant from the Isle of Man Anti Cancer Research Charity.

# Author Contribution

T.A. and M.L.M acquired most of the MR data; T.A., S.B., M.M. and M.L.M. contributed to data analysis; E.N.G. helped with maintaining cell lines and tumour implantations; S.A., M.M and M.S. helped with experiments related to Sea Horse Assay and generated relevant figures. L.R. helped with histological and immunohistochemical analysis as well as relevant figure. T.A., S.S., M.L.M and H.P. wrote the initial draft of the paper; M.M., M.S. and H.P. conceptualised and supervised the study. All authors reviewed, edited and approved the final manuscript.

# Acknowledgement

The authors acknowledge the use of the Centre for Preclinical Imaging (CPI) and Biobank facilities provided by Liverpool Shared Research Facilities (LIVSRF), University of Liverpool. We also acknowledge the Histology Laboratory, Leahurst Campus, University of Liverpool. Tareq Alrashidi has been funded by a PhD studentship grant from the Ministry of Education, Saudi Arabia. Sharifa Alyetama has been funded by a PhD studentship grant from the Ministry of Health, The State of Kuwait. The authors acknowledge Dr. Amy Chadwick (University of Liverpool) for assistance with the Seahorse experiments, Dr. Helen Kalrai for assistance with MCT4 IHC staining, Dr. Stephen Pickup (University of Pennsylvania, USA) for providing rhe Sel-MQC sequence and Dr. Sungheon G. Kim (Weill Cornell Medical College, USA) for providing GL261 cells.

# Data Availability

The datasets used and analysed for the current study is available from the corresponding author on reasonable request

## References

1. Stupp, R. et al. European Organisation for Research and Treatment of Cancer Brain Tumor and Radiotherapy Groups; National Cancer Institute of Canada Clinical Trials Group. Radiotherapy plus concomitant and adjuvant temozolomide for glioblastoma. *N Engl. J. Med.* **352** (10), 987–996. 10.1056/NEJMoa043330 (2005).
2. Zhang, J., Stevens, M. F. & Bradshaw, T. D. Temozolomide: mechanisms of action, repair and resistance. *Curr. Mol. Pharmacol.* **5** (1), 102–114. 10.2174/1874467211205010102 (2012).
3. Meany, H. J. et al. Pharmacokinetics of temozolomide administered in combination with O6-benzylguanine in children and adolescents with refractory solid tumors. *Cancer Chemother. Pharmacol.* **65** (1), 137–142. 10.1007/s00280-009-1015-8. (2009). Epub 2009 May 9. PMID: 19430790; PMCID: PMC6301000.

4. Dyrka, K. et al. Temozolomide: a cytostatic drug that is still important today. *Acta Pol. Pharm. - Drug Res.* 10.32383/appdr/159449 (2023).
5. Wang, N., Zhang, Q., Ning, B., Luo, L. & Fang, Y. β-Asarone promotes Temozolomide's entry into glioma cells and decreases the expression of P-glycoprotein and MDR1. *Biomed. Pharmacother*. **90**, 368–374 (2017). Epub 2017 Apr 2. PMID: 28380412.
6. White, J., White, M. P. J., Wickremesekera, A., Peng, L. & Gray, C. The tumour microenvironment, treatment resistance and recurrence in glioblastoma. *J. Transl Med.* **22** (1), 540. 10.1186/s12967-024-05301-9. (2024). PMID: 38844944; PMCID: PMC11155041.
7. Esteller, M. et al. Inactivation of the DNA-repair gene MGMT and the clinical response of gliomas to alkylating agents. *N Engl. J. Med.* **343** (19), 1350–1354. 10.1056/NEJM200011093431901 (2000).
8. Yan, C., Ge, Y., Hu, Z. & Ma, W. Targeting metabolic mechanisms to overcome temozolomide resistance in glioblastoma. *Discov Oncol.* **17** (1), 444. 10.1007/s12672-026-04572-6. (2026). PMID: 41677997; PMCID: PMC13000057.
9. Fu, M. et al. Use of Bevacizumab in recurrent glioblastoma: a scoping review and evi- dence map. *BMC Cancer*. **23**, 544. 10.1186/s12885-023-11043-6 (2023).
10. Alrashidi, T. et al. Evaluating the Combined Effect of a Choline Kinase Inhibitor and Temozolomide Therapy in a Mouse Model of Glioblastoma Using $^{1}$H MR Spectroscopy and IVIM-DWI. *NMR Biomed.* **38** (9), e70113. 10.1002/nbm.70113 (2025).
11. Sharma, P., Aaroe, A., Liang, J. & Puduvalli, V. K. Tumor microenvironment in glioblastoma: Current and emerging concepts. *Neurooncol Adv.* **5** (1), vdad009. 10.1093/noajnl/vdad009. (2023). PMID: 36968288; PMCID: PMC10034917.
12. Tamai, S. et al. Tumor Microenvironment in Glioma Invasion. *Brain Sci.* **12** (4), 505. 10.3390/brainsci12040505. (2022). PMID: 35448036; PMCID: PMC9031400.
13. Gatenby, R. A. & Gillies, R. J. Why do cancers have high aerobic glycolysis? *Nat. Rev. Cancer*. **4** (11), 891–899. 10.1038/nrc1478 (2004).
14. Ostermann, S. et al. Plasma and cerebrospinal fluid population pharmacokinetics of temozolomide in malignant glioma patients. *Clin. Cancer Res.* **10** (11), 3728–3736. 10.1158/1078-0432.CCR-03-0807 (2004).
15. Hamaguchi, R., Uemoto, S., Wada, H. & Editorial The impact of alkalizing the acidic tumor microenvironment to improve efficacy of cancer treatment. *Front. Oncol.* **13**, 1223025. 10.3389/fonc.2023.1223025 (2023).
16. Nath, K. et al. Mechanism of antineoplastic activity of lonidamine. *Biochim. Biophys. Acta*. **1866** (2), 151–162 (2016). Epub 2016 Aug 4. PMID: 27497601; PMCID: PMC5138080.
17. Xu, H. N. et al. Optical Redox Imaging of Lonidamine Treatment Response of Melanoma Cells and Xenografts. *Mol. Imaging Biol.* **21** (3), 426–435. 10.1007/s11307-018-1258-z (2019).
18. Huang, Y. et al. Energy Blocker Lonidamine Reverses Nimustine Resistance in Human Glioblastoma Cells through Energy Blockade, Redox Homeostasis Disruption, and $O^{6}$-Methylguanine-DNA

Methyltransferase Downregulation: *In Vitro* and *In Vivo* Validation. ACS Pharmacol Transl Sci. ;7(5):1518–1532. (2024). 10.1021/acsptsci.4c00085. PMID: 38751635; PMCID: PMC11092191.

19. Huang, Y. et al. The Potential of Lonidamine in Combination with Chemotherapy and Physical Therapy in Cancer Treatment. *Cancers (Basel)*. **12** (11), 3332. 10.3390/cancers12113332 (2020).
20. Nath, K. et al. Lonidamine induces intracellular tumor acidification and ATP depletion in breast, prostate and ovarian cancer xenografts and potentiates response to doxorubicin. *NMR Biomed.* **28** (3), 281–290. 10.1002/nbm.3240 (2015).
21. Li, Z., Munim, M. B., Sharygin, D. A., Bevis, B. J. & Vander Heiden, M. G. Understanding the Warburg Effect in Cancer. *Cold Spring Harb Perspect. Med.* **15** (12), a041532. 10.1101/cshperspect. a041532 (2025). PMID: 39284669; PMCID: PMC12667404.
22. Luengo, A. et al. Increased demand for $NAD^+$ relative to ATP drives aerobic glycolysis. *Mol. Cell.* **81** (4), 691–707e6 (2021). Epub 2020 Dec 30. PMID: 33382985; PMCID: PMC8315838.
23. Huggler, K. S. et al. Hexokinase detachment from mitochondria drives the Warburg effect to support compartmentalized ATP production. *Nat. Metab.* **8** (1), 215–236. 10.1038/s42255-025-01428-1. (2026). Epub 2026 Jan 16. PMID: 41545565; PMCID: PMC13137452.
24. Nath, K. et al. Impact of therapeutic inhibition of oncogenic cell signaling tyrosine kinase on cell metabolism: in vivo-detectable metabolic biomarkers of inhibition. *J. Transl Med.* **22** (1), 622. 10.1186/s12967-024-05371-9 (2024).
25. Gupta, P. K. et al. Metabolic Imaging Biomarkers of Response to Signaling Inhibition Therapy in Melanoma. *Cancers (Basel)*. **16** (2), 365. 10.3390/cancers16020365 (2024).
26. Yamada, T. et al. Riluzole enhances the antitumor effects of temozolomide via suppression of MGMT expression in glioblastoma. J Neurosurg. ;134(3):701–710. doi: 10.3171/2019.12.JNS192682. PMID: 32168477. (2020).
27. Park, J. et al. Effect of combined anti-PD-1 and temozolomide therapy in glioblastoma. *Oncoimmunology* **8** (1), e1525243 (2018). PMID: 30546966; PMCID: PMC6287793.
28. Carrano, A., Juarez, J. J., Incontri, D., Ibarra, A. & Guerrero Cazares, H. Sex-Specific Differences in Glioblastoma. *Cells* **10** (7), 1783. 10.3390/cells10071783. (2021). PMID: 34359952; PMCID: PMC8303471.
29. Bhaduri, S. et al. Metabolic changes in glioblastomas in response to choline kinase inhibition: In vivo MRS in rodent models. *NMR Biomed.* **36** (3), e4855. 10.1002/nbm.4855 (2023).
30. Nath, K. et al. Effect of Lonidamine on Systemic Therapy of DB-1 Human Melanoma Xenografts with Temozolomide. *Anticancer Res.* **37** (7), 3413–3421. 10.21873/anticanres.11708. (2017). PMID: 28668829; PMCID: PMC8757536.
31. Cen, L. et al. Efficacy of protracted temozolomide dosing is limited in MGMT unmethylated GBM xenograft models. *Neuro Oncol.* **15** (6), 735–746. 10.1093/neuonc/not010 (2013).
32. Miccoli, L. et al. Potentiation of lonidamine and diazepam, two agents acting on mitochondria, in human glioblastoma treatment. J Natl Cancer Inst. ;90(18):1400-6. (1998). 10.1093/jnci/90.18.1400. PMID: 9747871.

33. Nath, K. et al. Effect of Differences in Metabolic Activity of Melanoma Models on Response to Lonidamine plus Doxorubicin. *Sci. Rep.* **8** (1), 14654. 10.1038/s41598-018-33019-4. (2018). PMID: 30279592; PMCID: PMC6168452.
34. Orlovskiy, S. et al. Lonidamine Induced Selective Acidification and De-Energization of Prostate Cancer Xenografts: Enhanced Tumor Response to Radiation Therapy. *Cancers (Basel)*. **16** (7), 1384. 10.3390/cancers16071384. (2024). PMID: 38611062; PMCID: PMC11010960.
35. Robinson, C. G. et al. Effect of alternative temozolomide schedules on glioblastoma O(6)-methylguanine-DNA methyltransferase activity and survival. *Br. J. Cancer*. **103** (4), 498–504. 10.1038/sj.bjc.6605792. (2010). Epub 2010 Jul 13. PMID: 20628383; PMCID: PMC2939788.
36. Palmieri, D. et al. Profound prevention of experimental brain metastases of breast cancer by temozolomide in an MGMT-dependent manner. *Clin. Cancer Res.* **20** (10), 2727–2739. 10.1158/1078-0432.CCR-13-2588. (2014). Epub 2014 Mar 14. PMID: 24634373; PMCID: PMC4100541.
37. He, Q., Shungu, D. C., van Zijl, P. C., Bhujwalla, Z. M. & Glickson, J. D. Singlescan in vivo lactate editing with complete lipid and water suppression by selective multiple-quantum-coherence transfer (Sel-MQC) with application to tumors. *J. Magn. Reson. B*. **106**, 203–211 (1995).
38. Muruganandham, M., Koutcher, J. A., Pizzorno, G. & He, Q. In vivo tumor lactate relaxation measurements by selective multiple-quantum-coherence (Sel-MQC) transfer. *Magn. Reson. Med.* **52**, 902–906 (2004).
39. Stefan, D., Cesare, F. D. & Andrasescu, A. Quantitation of magnetic resonance spectroscopy signals: the jMRUI software package. *Meas. Sci. Technol.* **20** (10), 035–104. 10.1088/0957-0233/20/10/104035 (2009).
40. Vanhamme, L., Fierro, R. D., Van Huffel, S. & De Beer, R. Fast removal of residual water in proton spectra. *J. Magn. Reson.* **132** (2), 197–203. 10.1016/0022-2364(92)90241-X (1998).
41. Pijnappel, W., Vandenboogaart, A., De Beer, R. & Van Ormondt, D. SVD- based quantification of magnetic-resonance signals. *J. Magn. Reson.* **97** (1), 122–134. 10.1016/0022-2364(92)90241-X (1992).
42. Graverondemilly, D., Diop, A., Briguet, A. & Fenet, B. Product-operator algebra for strongly coupled spin systems. *J. Magn. Reson. A*. **101** (3), 233–239. 10.1006/jmra.1993.1038 (1993).
43. Ratiney, H. et al. Time-domain semi-parametric estimation based on a metabolite basis set. *NMR Biomed.* **18** (1), 1–13. 10.1006/jmre.1998.1425 (2005).
44. Ratiney, H., Coenradi, Y., Cavassila, S., Ormondt, D. V. & Graveron-Demilly, D. Time-domain quantitation of 1H short echo-time signals: background ac- commodation. *Magn. Reson. Mater. Phys. Biol. Med.* **16** (6), 284–296 (2004).
45. Bhaduri, S. et al. Assessing Tumour Haemodynamic Heterogeneity and Response to Choline Kinase Inhibition Using Clustered Dynamic Contrast Enhanced MRI Parameters in Rodent Models of Glioblastoma. *Cancers (Basel)*. **14**, 1223–1223. 10.3390/cancers14051223 (2022).

46. Federau, C., Maeder, P., O'brien, K., Browaeys, P., Meuli, R., and Hagmann,P.(2012) Quantitative measurement of brain perfusion with intravoxel incoherent motion MR imaging. Radiology, 265 (3), 874–81, doi:10.1148/radiol.12120584.
47. Yoo, I., Ahn, I., Lee, J. & Lee, N. Extracellular flux assay (Seahorse assay): Diverse applications in metabolic research across biological disciplines. *Mol. Cells*. **47** (8), 100095. 10.1016/j.mocell.2024.100095. (2024). Epub 2024 Jul 18. PMID: 39032561; PMCID: PMC11374971.
48. Davy, M. et al. Evaluation of Temozolomide and Fingolimod Treatments in Glioblastoma Preclinical Models. *Cancers (Basel)*. **15** (18), 4478. 10.3390/cancers15184478. (2023). PMID: 37760448; PMCID: PMC10527257.
49. Mookerjee, S. A., Gerencser, A. A., Nicholls, D. G. & Brand, M. D. Quantifying intracellular rates of glycolytic and oxidative ATP production and consumption using extracellular flux measurements. J Biol Chem. ;292(17):7189–7207. doi: 10.1074/jbc.M116.774471. Epub 2017 Mar 7. Erratum in: J Biol Chem. 2018;293(32):12649–12652. (2017). 10.1074/jbc.AAC118.004855. PMID: 28270511; PMCID: PMC5409486.
50. Jia, D., Park, J. H., Jung, K. H., Levine, H. & Kaipparettu, B. A. Elucidating the Metabolic Plasticity of Cancer: Mitochondrial Reprogramming and Hybrid Metabolic States. *Cells* **7** (3), 21. 10.3390/cells7030021 (2018).
51. Pusapati, R. V. et al. mTORC1-Dependent Metabolic Reprogramming Underlies Escape from Glycolysis Addiction in Cancer Cells. *Cancer Cell.* **29** (4), 548–562. 10.1016/j.ccell.2016.02.018 (2016). Epub 2016 Mar 24.
52. Viale, A. et al. Oncogene ablation-resistant pancreatic cancer cells depend on mitochondrial function. *Nature* **514** (7524), 628–632. 10.1038/nature13611 (2014).
53. Altman, B. J., Stine, Z. E. & Dang, C. V. From Krebs to clinic: glutamine metabolism to cancer therapy. Nat Rev Cancer. ;16(10):619 – 34. doi: 10.1038/nrc.2016.71. Epub 2016 Jul 29. Erratum in: Nat Rev Cancer. 2016;16(12):773. (2016). 10.1038/nrc.2016.131
54. Guo, L. et al. Inhibition of Mitochondrial Complex II by the Anticancer Agent Lonidamine. *J. Biol. Chem.* **291** (1), 42–57. 10.1074/jbc.M115.697516 (2016).
55. Kaina, B., Christmann, M., Naumann, S. & Roos, W. P. MGMT: key node in the battle against genotoxicity, carcinogenicity and apoptosis induced by alkylating agents. *DNA Repair. (Amst)*. **6** (8), 1079–1099. 10.1016/j.dnarep.2007.03.008 (2007).
56. Oliva, C. R., Moellering, D. R., Gillespie, G. Y. & Griguer, C. E. Acquisition of chemoresistance in gliomas is associated with increased mitochondrial coupling and decreased ROS production. *PLoS One*. **6** (9), e24665. 10.1371/journal.pone.0024665. (2011). Epub 2011 Sep 9. PMID: 21931801; PMCID: PMC3170372.
57. Giglio, E., Giuseffi, M., Picerno, S., Sichetti, M. & Mecca, M. Optimised Workflows for Profiling the Metabolic Fluxes in Suspension vs. Adherent Cancer Cells via Seahorse Technology. *Int. J. Mol. Sci.* **26** (1), 154. 10.3390/ijms26010154 (2024).

58. Cervantes-Madrid, D. et al. Feasibility and antitumor efficacy in vivo, of simultaneously targeting glycolysis, glutaminolysis and fatty acid synthesis using lonidamine, 6-diazo-5-oxo-L-norleucine and orlistat in colon cancer. *Oncol. Lett.* **13** (3), 1905–1910. 10.3892/ol.2017.5615 (2017).
59. Jabehdar Maralani, P. et al. Intravoxel incoherent motion (IVIM) modeling of diffusion MRI during chemoradiation predicts therapeutic response in IDH wildtype glioblastoma. *Radiother Oncol.* **156**, 258–265. 10.1016/j.radonc.2020.12.037 (2021).
60. Ben-Yoseph, O., Lyons, J. C., Song, C. W. & Ross, B. D. Mechanism of action of lonidamine in the 9L brain tumor model involves inhibition of lactate efflux and intracellular acidification. J Neurooncol. ;36(2):149 – 57. (1998). 10.1023/a:1005819604858. PMID: 9525814.
61. Virrey, J. J. et al. Glioma-associated endothelial cells are chemoresistant to temozolomide. *J. Neurooncol*. **95** (1), 13–22. 10.1007/s11060-009-9891-7. (2009). Epub 2009 Apr 18. PMID: 19381445.
62. Stéphanou, A. & Ballesta, A. pH as a potential therapeutic target to improve temozolomide antitumor efficacy: A mechanistic modeling study. *Pharmacol. Res. Perspect.* **7** (1), e00454. 10.1002/prp2.454 (2019).
63. Paech, D. et al. Whole-Brain Intracellular pH Mapping of Gliomas Using High-Resolution 31P MR Spectroscopic Imaging at 7.0 T. *Radiol. Imaging Cancer*. **6** (1), e220127. 10.1148/rycan.220127 (2024).
64. Pu, J. et al. Glioblastoma multiforme: an updated overview of temozolomide resistance mechanisms and strategies to overcome resistance. *Discov Oncol.* **16** (1), 731. 10.1007/s12672-025-02567-3 (2025).
65. Brawanski, K. R. et al. Influence of MMR, MGMT Promotor Methylation and Protein Expression on Overall and Progression-Free Survival in Primary Glioblastoma Patients Treated with Temozolomide. *Int. J. Mol. Sci.* **24** (7), 6184. 10.3390/ijms24076184 (2023).
66. Papacocea, S. I. et al. Molecular Profile as an Outcome Predictor in Glioblastoma along with MRI Features and Surgical Resection: A Scoping Review. *Int. J. Mol. Sci.* **25** (17), 9714. 10.3390/ijms25179714 (2024).
67. Lu, C. et al. DNA Sensing in Mismatch Repair-Deficient Tumor Cells Is Essential for Anti-tumor Immunity. *Cancer Cell.* **39** (1), 96–108e6. 10.1016/j.ccell.2020.11.006 (2021).
68. Sui, Y., Shen, Z., Wang, Z., Feng, J. & Zhou, G. Lactylation in cancer: metabolic mechanism and therapeutic strategies. *Cell. Death Discov*. **11** (1), 68. 10.1038/s41420-025-02349-4. (2025). PMID: 39979245; PMCID: PMC11842571.

# Tables

Table 1 and 2 are available in the Supplementary Files section.

# Figures

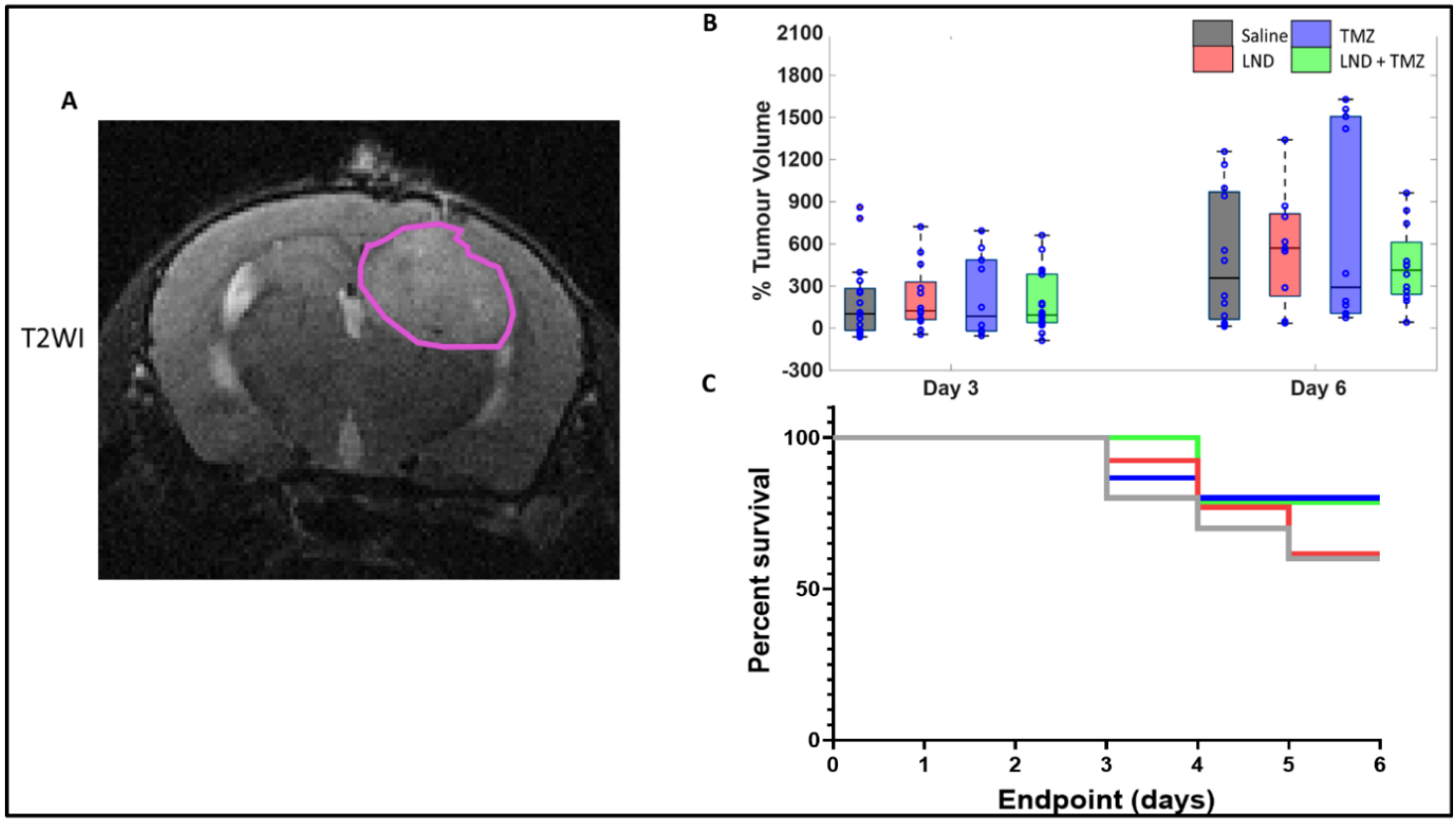



**Figure 1**

A. Representative axial $T_2$-weighted MR image from a mouse with a delineated tumour region of interest (magenta). B. Box plots showing percent change in tumour volume relative to baseline on days 3 and 6 across treatment groups. C. Kaplan-Meier survival curves showing the percentage survival for each treatment group.

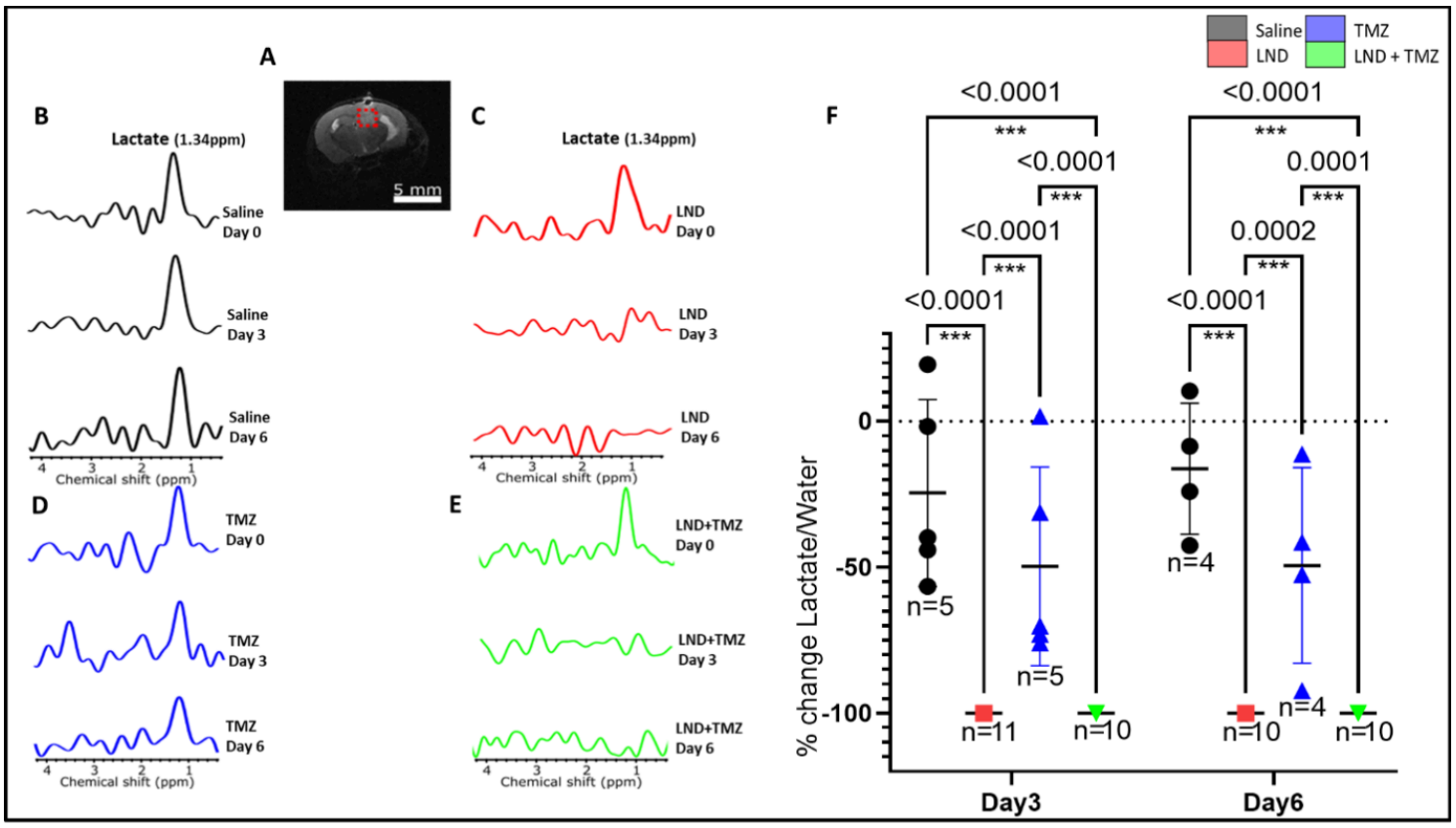



**Figure 2**

A-F: Representative position of a spectroscopic voxel (red) overlaid on a $T_2$-weighted image (A). Lactate-edited ISIS-selMQC spectra from each treatment group on days 0, 3 and 6 (B-E). Percentage change in lactate/water ratio, measured at day 3 and day 6, relative to day 0, for all experimental groups (F). Asterisks indicate the difference between groups where $p<0.05$.

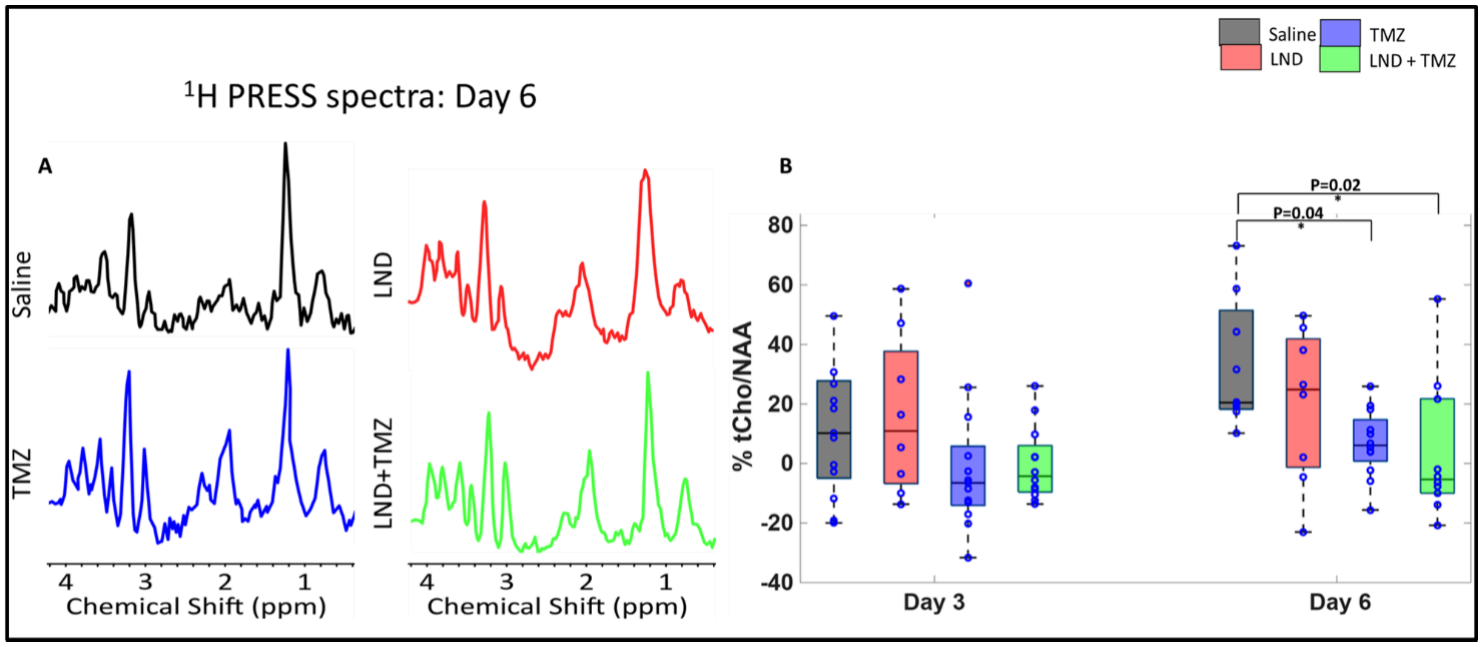



**Figure 3**

A-B: Representative $^{1}$H-MRS PRESS spectra acquired from tumours in each treatment group on day 6 (A). Box plots of percentage change in tCho/NAA ratios on days 3 and 6, relative to day 0, across groups (B). Asterisks indicate the difference between groups where $p<0.05$.

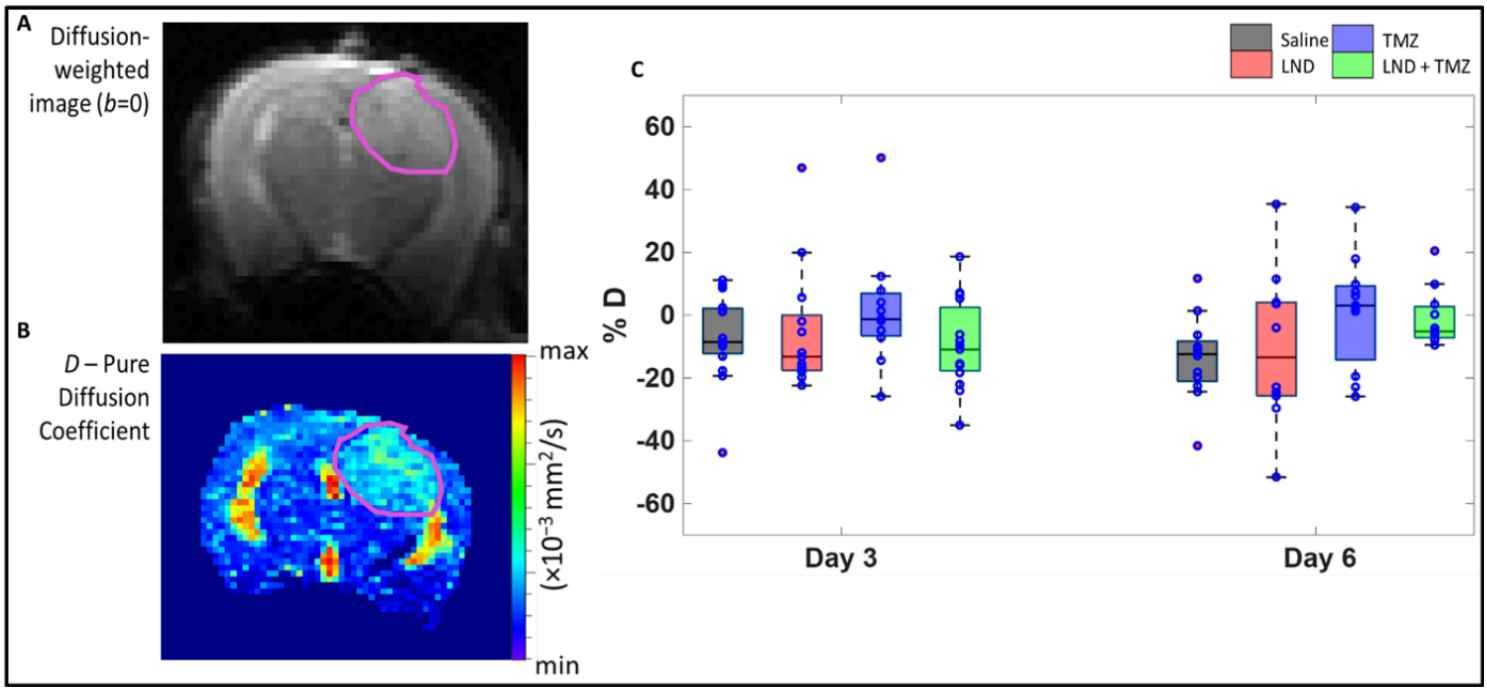
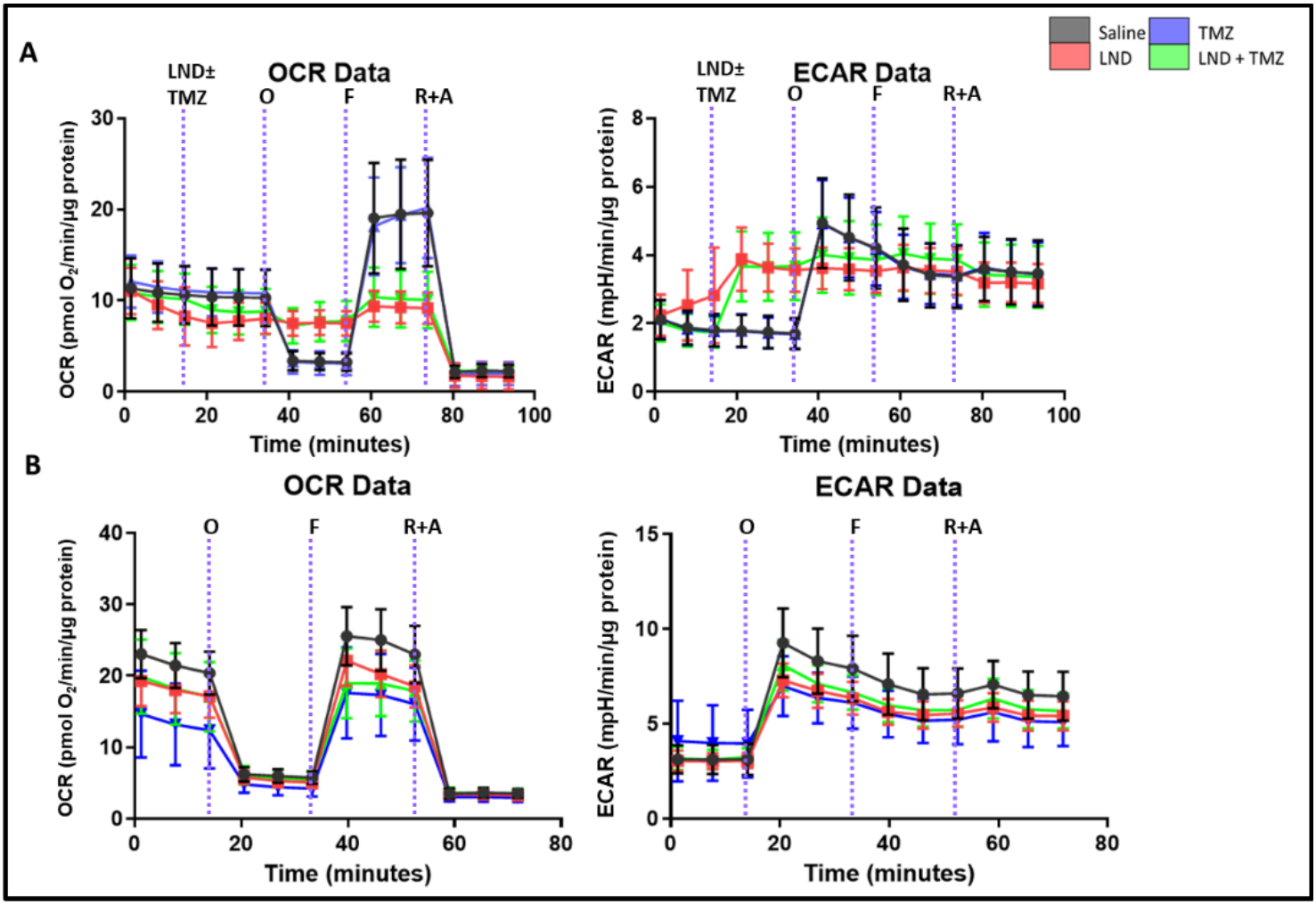



**Figure 4**

IVIM-DWI-derived diffusion parameters across treatment groups. (**A**) Representative IVIM image (b=0 s/mm$^2$) with tumour margin indicated (magenta). (**B**) Parametric map of the pure diffusion coefficient (*D*). (**C**) Box plots illustrating the percentage change in *D* relative to day 0 within tumours for all experimental groups at days 3 and 6 post-treatment.




## Figure 5

Representative Seahorse XFe96 Mito Stress Test profiles illustrating (A) the acute (~30 min) and (B) chronic (72 h) effects of Lonidamine (LND), Temozolomide (TMZ), and their combination on GL261 glioblastoma cells. Oxygen Consumption Rate (OCR) and Extracellular Acidification Rate (ECAR) were measured in real time to assess mitochondrial respiration and glycolytic activity, respectively. Cells were pre-treated with LND, TMZ, or LND + TMZ prior to sequential injections of Oligomycin (O; 1 µM), FCCP (F; 0.5 µM), and a combined Rotenone/Antimycin A solution (R+A; 1 µM each), as indicated by the vertical dotted lines.

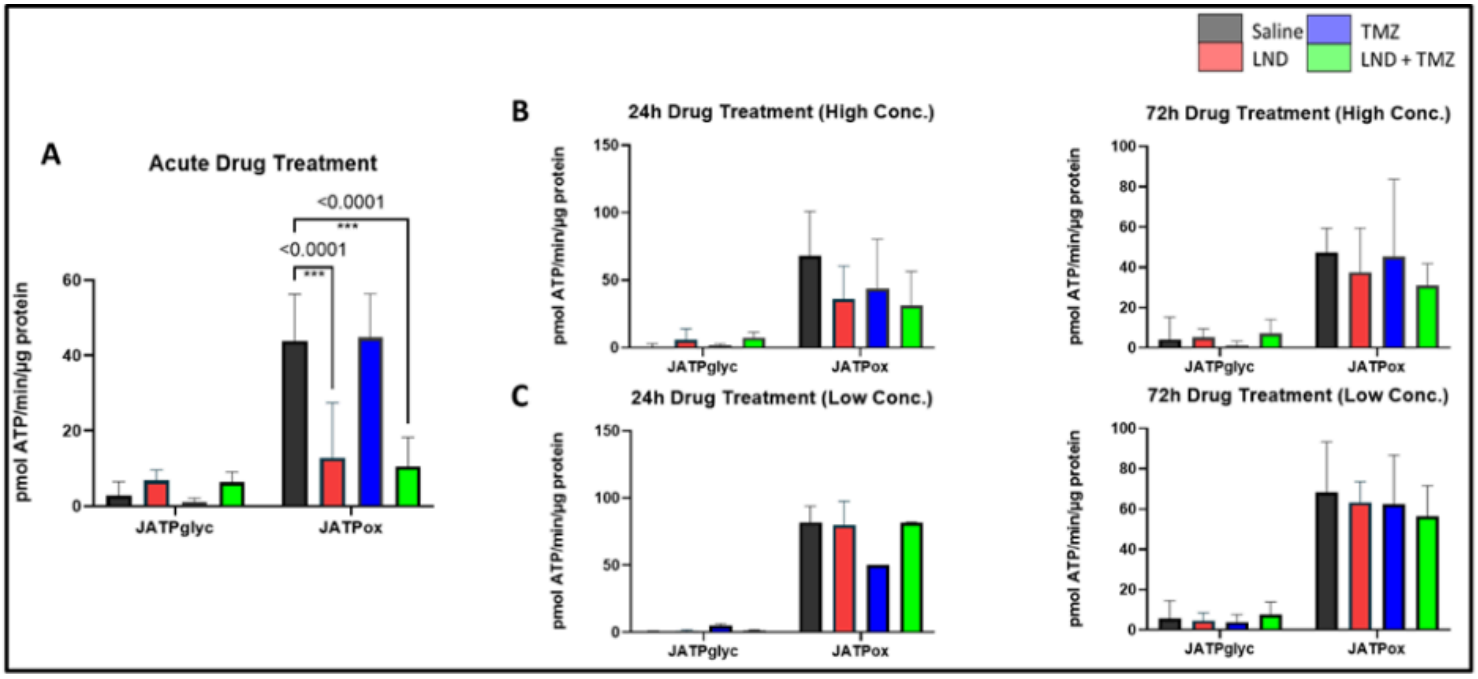
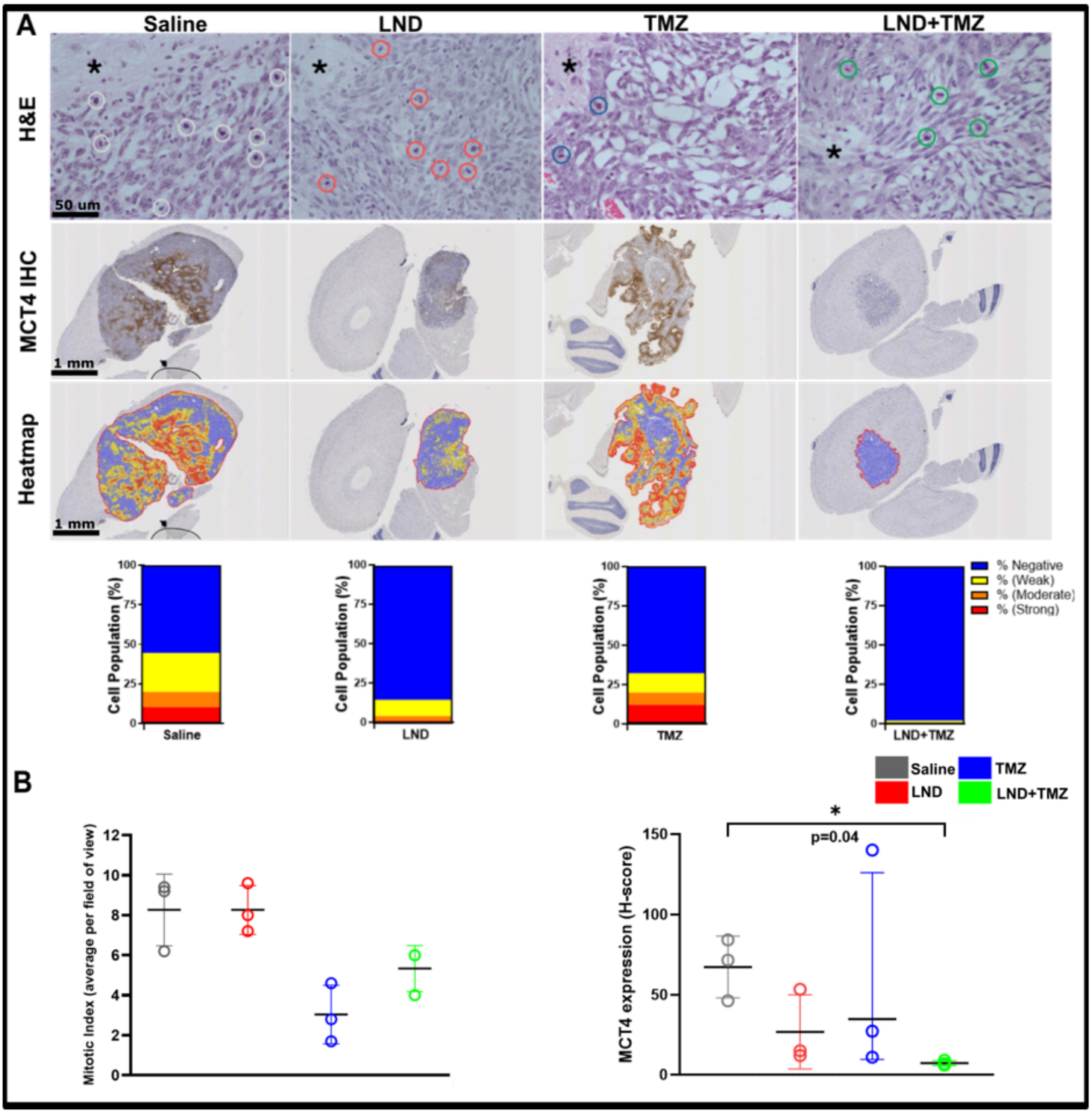



**Figure 6**

A-B: Acute and chronic effects of lonidamine and temozolomide on mitochondrial and glycolytic ATP production. Bar graphs show ATP production rates derived from glycolysis (JATPglyc) and oxidative phosphorylation (JATPox) in untreated control (Ctrl) cells and in cells treated acutely (~30 min) (A) or for 24 h (B) and 72 h (C) at high and low drug concentrations with lonidamine (LND), temozolomide (TMZ), or their combination (LND + TMZ). ATP production rates are expressed as pmol ATP/min/µg$^{-1}$ protein and presented as mean ±SD of biological replicates (acute n=4, chronic n=3), normalised to total protein content. Significance levels are indicated by asterisks.




## Figure 7

A-B: Evaluation of tumour proliferation and MCT4 expression. Micrographs are arranged by treatment group (columns). (A) Top row:Representative haematoxylin–eosin (H&E, 400x) sections showing tumour morphology; circles highlight mitotic figures, and normal brain parenchyma is indicated (*). Second Row: Immunohistochemical (IHC) staining for MCT4 (brown) from the whole brain sections including the tumour. Third Row: Corresponding QuPath-generated staining intensity heatmaps. Bottom Row: Cell distribution analysis. Stacked bar charts represent the percentage of total cells categorized by staining

intensity: Blue = Negative (no staining); Yellow to Red = increasing staining intensity reflecting MCT4 protein concentration. (B) Groupwise distribution of mitosis and MCT4 expression. Scatter plots showing individual sample data (n=3) for Mitotic Index (left) and MCT4 H-score (right). The asterisk indicates the difference between groups where $p<0.05$.

## Supplementary Files

This is a list of supplementary files associated with this preprint. Click to download.

- Tables12.docx